Monthly Notices
of the
ROYAL ASTRONOMICAL SOCIETY

Mon. Not. R. Astron. Soc. **426,** 427–439 (2012) doi:10.1111/j.1365-2966.2012.21394.x

White dwarf kinematics versus mass

Christopher Wegg⋆ and E. Sterl Phinney

Department of Physics, Mathematics and Astronomy, MC 350-17, California Institute of Technology, Pasadena, CA 91125, USA

Accepted 2012 May 24. Received 2012 May 24; in original form 2011 July 4

ABSTRACT

We investigated the relationship between the kinematics and mass of young ($<3 \times 10^8$ yr) white dwarfs using proper motions. Our sample is taken from the colour-selected catalogues of the Sloan Digital Sky Survey and the Palomar–Green Survey, both of which have spectroscopic temperature and gravity determinations. We find that the dispersion decreases with increasing white dwarf mass. This can be explained as a result of less scattering by objects in the Galactic disc during the shorter lifetime of their more massive progenitors. A direct result of this is that white dwarfs with high mass have a reduced scale height, and hence their local density is enhanced over their less massive counterparts. In addition, we have investigated whether the kinematics of the highest mass white dwarfs ($>0.95\,M_\odot$) are consistent with the expected relative contributions of single star evolution and mergers. We find that the kinematics are consistent with the majority of high-mass white dwarfs being formed through single star evolution.

Key words: white dwarfs – Galaxy: kinematics and dynamics.

1 INTRODUCTION

Despite the significant work on both the kinematics and mass distribution of white dwarfs (WDs), very little work has addressed their connection.

The kinematics of galactic WDs have been studied on numerous occasions with several motivations. They have proven useful in attempts to unravel the evolutionary history and progenitors of the various classes of WDs (Sion et al. 1988; Anselowitz et al. 1999). Interest in WD kinematics was also prompted by the suggestion that halo WDs could provide a significant contribution to Galactic dark matter (Oppenheimer et al. 2001; Reid 2005). This effort has concentrated on the identification of halo WDs and estimating the resultant density, which now appears to be a small contribution to the Galactic dark matter budget (Pauli et al. 2006). Moreover, the mass distribution of the most common hydrogen-rich (DA) WDs has also been extensively investigated, particularly for WDs with $T \gtrsim 10\,000$ K which are hot enough for their masses to be deduced spectroscopically from fits to their Balmer lines (Vennes 1999; Liebert et al. 2005; Kepler et al. 2007). The mass distribution shows a peak at $0.6\,M_\odot$ due to the relative abundance of their lower mass progenitors with a tail extending to higher masses formed from more massive progenitors.

The connection between the galactic kinematics of a group of thin disc objects and their progenitors is largely due to the process of kinematic disc 'heating' (Wielen 1977; Nordström et al. 2004). The hot WDs with short cooling ages we observe in the galactic neighbourhood today are formed from a wide range of progenitor masses ($\sim$0.8–8 $M_\odot$) and hence have a wide range in age. We therefore expect high-mass disc WDs to have a low velocity dispersion in comparison to low-mass disc WDs whose progenitors formed earlier. This connection was suggested in Guseinov, Novruzova & Rustamov (1983) who performed an analysis suggesting that WDs with larger masses have smaller dispersions; however, this was reinvestigated by Sion et al. (1988) with a larger sample of 78 DA WDs where no evidence for any correlation was found. This paper readdresses the connection between mass and kinematics with a greatly increased sample size.

The outline of the paper is as follows. In Section 2, we discuss the sample selection and the calculation of distances and proper motions. In Section 3, we discuss how we estimate the kinematics of the sample without radial velocity information. We use two methods, that of Dehnen & Binney (1998) (Section 3.1) and a Markov Chain Monte Carlo (MCMC), where we marginalize over the unknown radial velocity (Section 3.2). In Section 4, we analyse whether the kinematics are consistent with single star evolution (SSE) both via analytic methods (Section 4.1) and simulations (Section 4.2). In Section 5, we analyse whether the highest mass WDs are largely formed through SSE or are the product of the merger of two lower mass WDs. Finally, we discuss the implications of our findings on the scale height of WDs in Section 6.

For the reader in a hurry, the primary result of this paper, the relationship between the mass of young WDs and their velocity dispersion, is shown in Fig. 3 and discussed in Section 3. The implied scale heights, the second key result, are then discussed in Section 6. These results have been checked using a Monte Carlo simulation of the formation and observation of an ensemble of WDs,

⋆E-mail: wegg@tapir.caltech.edu

Table 1. Summary of the sample.

	PG	SDSS
Number of DA white dwarfs with good photometry not known to be binaries	299	6926
of these number with signal-to-noise >10	299	3125
of these number with 13 000 K < $T_{\rm eff}$ < 40 000 K	215	1555
of these number with age $<3 \times 10^8$ yr	211	1491
Distance source:		
Liebert et al. (2005)	79	0
SDSS photometry	132	1491
of these numbers rejected with $\chi^2 > 5$	0	48
Proper motion source:		
Munn et al. (2008)	153	1443
PPMXL	54	0
Manual measurement from POSS I/II	4	0

which is described by flowcharts in Figs 6–8: in Fig. 6 the process of choosing stars is described, in Fig. 7 the process of placing them in the disc is described and in Fig. 8 the process of determining the observability of the simulated WD is described.

2 SAMPLE

We investigate only hydrogen atmosphere (DA) WDs due to the relative simplicity of their spectra and the resultant security of the spectroscopic masses. The sample of DA WDs is taken from two sources, the Palomar–Green (PG) white dwarf survey (Liebert et al. 2005) and the Sloan Digital Sky Survey (SDSS) DR4 white dwarf survey (Eisenstein et al. 2006). The SDSS sample is much larger than the PG sample. The PG sample is included as a demonstration that the results are secure, and not a result of systematics in the SDSS, such as the complex selection of targets. For clarity, we first discuss which types of WDs we select, then discuss how the SDSS is dealt with, and finally how the PG survey was dealt with. The sample and its selection are summarized in Table 1.

2.1 Selected WDs

Both PG and SDSS are colour selected, eliminating the kinematic biases inherent in proper motion-based surveys, and contain spectroscopic determinations of surface gravity, $\log g$, and effective temperature, $T_{\rm eff}$, obtained by fitting the profile of the Balmer lines. We restrict the sample to objects whose fitted $T_{\rm eff}$ was between 13 000 and 40 000 K, since $\log g$ appears to be systematically overestimated at low temperatures and $T_{\rm eff}$ overestimated at higher temperatures (Eisenstein et al. 2006).

The fitted $\log g$ and $T_{\rm eff}$ are converted to masses and ages using the carbon core WD cooling models of Fontaine, Brassard & Bergeron (2001) below 30 000 K and Wood (1995) with thick hydrogen layers of fractional mass 10^{-4} above 30 000 K.[1] WDs with inferred masses less than 0.47 $M_\odot$ are instead assumed to have helium cores whose masses and ages are calculated from the models of Serenelli et al. (2001). Only objects with cooling ages below 3×10^8 yr are included in the sample to avoid significant kinematic heating after WD formation. The requirements of cooling age below 3×10^8 yr and $T_{\rm eff}$ above 13 000 K are competing. Above 0.60 $M_\odot$, the WDs cool more slowly and thus the age limit is used, while below 0.60 $M_\odot$ the temperature limit is used.

WDs previously discussed in the literature as known members of binaries were removed from the samples.

2.2 SDSS (Eisenstein et al. 2006)

Many of the SDSS spectra have low signal-to-noise ratios and hence large errors on their fitted $\log g$ and $T_{\rm eff}$. To ensure accurate masses and photometric distances, only objects whose spectra had a signal-to-noise ratio larger than 10 are included. The grid of model atmospheres fitted in the SDSS catalogue extends only to $\log g = 9$, and thus, for objects at this limit, the refitted $\log g$ and $T_{\rm eff}$ given in Kepler et al. (2007) were used.

Photometric distances to the WDs in the SDSS are calculated by minimizing

$$\chi^2 = \sum_{i=(u,g,r,i,z)} (m_i - [M_i(\log g, T_{\rm eff}) + A_g a_i + 5\log d - 5])^2/\sigma_i^2, \quad (1)$$

where m_i and σ_i are the five-band SDSS photometry and their errors, M_i are the model absolute magnitudes, $A_g a_i$ is the reddening and d the distance in parsecs.The error σ_i is the quoted photometric error in SDSS each band added in quadrature to a systematic error of $(u, g, r, i, z) = (0.015, 0.007, 0.007, 0.007, 0.01)$ (Kleinman et al. 2004). Model absolute magnitudes are taken from the atmospheric models provided by Bergeron (see footnote 1). $A_g a_i$ is the product of $R_V = 3.1$ extinction in each band of $(a_u, a_g, a_r, a_i, a_z) = (1.36, 1.00, 0.73, 0.55, 0.39)$ and the overall extinction A_g, which is constrained to lie between zero and the value of the galactic extinction map of Schlegel, Finkbeiner & Davis (1998) at the position of the object considered.

The resulting distribution of χ^2 values calculated by minimizing equation (1) is plotted in Fig. 1. It closely resembles a χ^2 distribution, but with an extended tail. Objects with reduced χ^2 larger than 5 were removed from the sample; most of these objects show an excess towards the redder photometric bands, indicating that they are in binaries with a cooler WD companion. Errors in the photometric distance are taken to be the $\Delta\chi^2 = 1$ surface added in quadrature

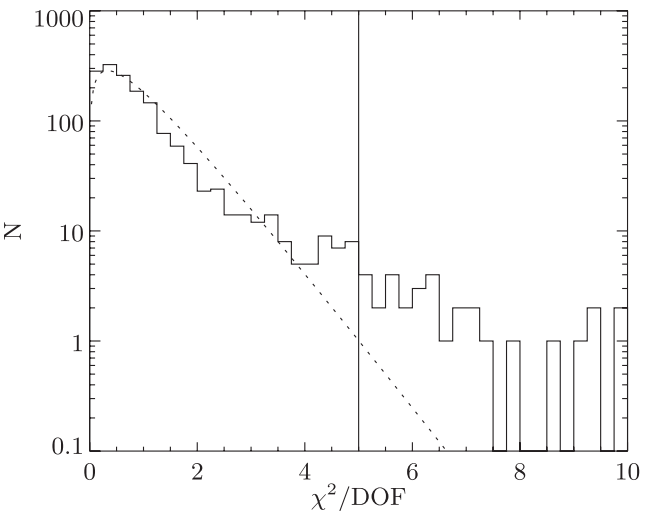

Figure 1. χ^2 per degree of freedom (DOF) for the fitted photometric distance of the 1443 SDSS DA WDs considered. A χ^2 function with three DOF is plotted as the dotted line. Beyond $\chi^2 = 5$, the WDs are rejected.

[1] Available from http://www.astro.umontreal.ca/bergeron/CoolingModels/, uses results from Holberg & Bergeron (2006), Kowalski & Saumon (2006), Tremblay, Bergeron & Gianninas (2011) and Bergeron et al. (2011).

to the distance errors introduced though the uncertainty in $\log g$ and $T_{\rm eff}$.

Proper motions for the SDSS sample are taken from the catalogue of Munn et al. (2008). These proper motions are calculated from the USNO-B1.0 plate positions re-calibrated using nearby galaxies together with the SDSS position so that the proper motions are more accurate and absolute. By measuring the proper motions of quasars, Munn et al. (2004) estimate that the 1σ error is 5.6 mas yr^{-1}.

2.3 PG survey

For 132 stars in the PG survey, SDSS photometry was available and the same method was used as for SDSS stars. For the remaining objects, the PG catalogue photometric distances were used. These were estimated in Liebert et al. (2005) from comparison of the V-band magnitude with the predicted M_V from the same models of Holberg & Bergeron (2006). Comparison of the stellar distances given by the two methods gives a standard deviation of 7 per cent. The majority of this error is expected to be in the PG survey distances and hence a conservative 10 per cent error was applied to these.

Proper motions for PG WDs that appear in the SDSS are taken from the catalogue of Munn et al. (2008). For the remaining objects, the PPMXL proper motion was used where available, which has a typical 1σ error of $\sim$8 mas yr^{-1}(Roeser, Demleitner & Schilbach 2010).

Finally, four objects in the PG sample have no reliable PPMXL proper motion, primarily due to a spurious matching of objects between epochs. For these, the proper motion was calculated directly between the scanned Palomar Observatory Sky Survey (POSS)-I and POSS-II plates. The proper motion was measured relative to nearby faint stars of similar magnitude corrected for galactic rotation (see Section 3.1). Typical errors estimated from the proper motions of stars of similar magnitude to be 11 mas yr^{-1}. We emphasize that only 4 of 1491 WDs use this method, and none have mass above 0.95 $M_\odot$ analysed in more detail in Section 5.

2.4 Final sample

The resulting sample of 1443 SDSS and 211 PG WDs contains young DA WDs with reliable masses, proper motions and photometric distances. The mass distribution of the samples is shown in Fig. 2. The process of constructing the sample together with numbers of objects is summarized in Table 1.

3 KINEMATICS WITHOUT RADIAL VELOCITIES

We now turn to calculating the mean velocity and the velocity dispersion for our sample. While radial velocities are required to completely determine the kinematics of an individual object, bulk kinematic properties such as the mean velocity and the velocity dispersion can be determined from only transverse motions.

We use two methods to do so, the frequentist method used in Section 3.1 and an MCMC in Section 3.2. Both methods give similar results which are summarized in Table 2.

3.1 Method of Dehnen & Binney (1998)

The method used here is adapted from Dehnen & Binney (1998). First the observed proper motions in galactic coordinates, $\mu_\ell^{\rm obs}$ and

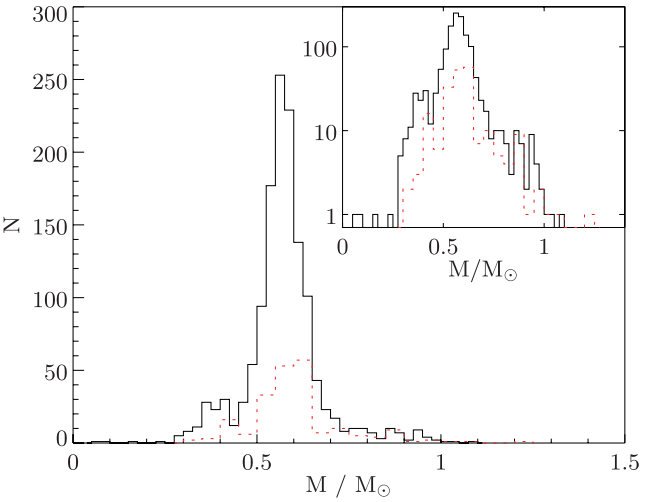

Figure 2. Mass distribution of the samples of the SDSS (black line) and PG (dashed red line) WDs after the cuts described in the text. The inset graph shows the same data on logarithmic axes.

$\mu_b^{\rm obs}$, are corrected for Galactic rotation through

$$\mu_\ell = \mu_\ell^{\rm obs} - A\cos(2\ell) - B$$
$$\mu_b = \mu_b^{\rm obs} + A\sin(2\ell)\cos b\sin b, \qquad (2)$$

using $A = 14.82\,{\rm km\,s^{-1}\,kpc^{-1}}$ and $B = -12.37\,{\rm km\,s^{-1}\,kpc^{-1}}$ (Feast & Whitelock 1997). In galactic coordinates where the components are directed towards the galactic centre, in the direction of galactic rotation and towards the north Galactic pole, we observe the velocity

$$\boldsymbol{V}_\perp = 4.74\,d \begin{bmatrix} -\mu_\ell\,\sin\ell\,\cos b - \mu_b\,\cos\ell\,\sin b \\ \mu_\ell\,\cos\ell\,\cos b - \mu_b\,\sin\ell\,\sin b \\ \mu_b\,\cos b \end{bmatrix} {\rm km\,s^{-1}}, \qquad (3)$$

with d in kpc and proper motions in mas yr^{-1}. This is the projection of the velocity $\boldsymbol{V}$ on to the sky plane though the projection matrix

$$\boldsymbol{V}_\perp = \mathbf{A}\cdot\boldsymbol{V}\,, \quad \mathbf{A} = \mathbf{I} - \hat{\boldsymbol{r}}\otimes\hat{\boldsymbol{r}}, \qquad (4)$$

where $\hat{\boldsymbol{r}}$ is the unit vector to the star.

Next the quantity S^2 is formed through

$$S^2(\boldsymbol{V_0}) \equiv \left\langle |\boldsymbol{V}_\perp - \mathbf{A}\cdot\boldsymbol{V_0}|^2 \right\rangle. \qquad (5)$$

Under the assumption that the positions of the observed objects are uncorrelated with the velocity, the choice of $\boldsymbol{V_0}$ that minimizes S^2 is the mean velocity. Also S^2 at the minimum is a measure of the dispersion of the group.

Dehnen & Binney (1998) then calculate all independent six elements of the dispersion tensor. Unfortunately, this entails estimating nine parameters which limits its use to samples with large numbers of objects. This would require excessively wide bins for the high-mass region where there are few objects. Instead we choose to make further assumptions about the objects' velocities in order to reduce the number of fitted parameters. The mean velocity of each group towards the galactic centre and the north Galactic pole is simply a result of the solar motion and we take these to be 10.00 and 7.17 km s^{-1}, respectively (Dehnen & Binney 1998). The mean velocity in the direction of galactic rotation, $\boldsymbol{V_0}$, is kept as a free parameter since in addition to the solar motion this varies between groups due to the asymmetric drift. We also assume that

Table 2. Kinematic fitting results from the PG and SDSS samples described in Section 2 using the methods of Sections 3.1 and 3.2. $M_{\rm low}$ and $M_{\rm high}$ are in units of $M_\odot$, while σ_1 and V are in $\mathrm{km\,s^{-1}}$. N is the number of WDs in each mass bin.

		PG					SDSS			
			Dehnen & Binney (1998)		MCMC			Dehnen & Binney (1998)		MCMC	
$M_{\rm low}$	$M_{\rm high}$	N	σ_1	V	σ_1	V	N	σ_1	V	σ_1	V
0.30	0.40	5	47 ± 12	22 ± 13	48 ± 10	18 ± 12	70	53 ± 3	33 ± 4	40 ± 3	34 ± 4
0.40	0.47	20	49 ± 6	27 ± 7	49 ± 7	28 ± 6	62	68 ± 4	38 ± 6	70 ± 6	38 ± 6
0.47	0.55	35	47 ± 4	18 ± 6	51 ± 4	17 ± 4	333	56 ± 1	34 ± 2	57 ± 2	34 ± 2
0.55	0.60	53	37 ± 2	17 ± 3	40 ± 3	18 ± 3	482	46 ± 1	20 ± 1	45 ± 1	21 ± 1
0.60	0.65	51	37 ± 2	16 ± 3	34 ± 2	15 ± 2	239	33 ± 1	20 ± 1	31 ± 1	20 ± 1
0.65	0.75	23	33 ± 3	15 ± 4	34 ± 4	14 ± 5	91	26 ± 1	16 ± 2	28 ± 1	15 ± 1
0.75	0.85	9	16 ± 2	11 ± 4	17 ± 3	11 ± 4	30	16 ± 1	11 ± 2	19 ± 2	11 ± 2
0.85	0.95	10	12 ± 2	15 ± 2	12 ± 2	13 ± 2	28	18 ± 1	12 ± 2	19 ± 2	11 ± 2
0.95	1.44	5	22 ± 5	14 ± 7	24 ± 6	12 ± 6	9	19 ± 3	9 ± 5	24 ± 5	9 ± 6

the dispersion tensor takes the form

$$\boldsymbol{\sigma} = \sigma_1 \mathrm{diag}\left(1, \frac{1}{1.4}, \frac{1}{2.2}\right), \tag{6}$$

which is accurate for main sequence stars in the solar neighbourhood (Dehnen & Binney 1998). This reduces the number of parameters for each group to the asymmetric drift $\boldsymbol{V_0}$ and the normalization of the dispersion tensor σ_1.

$\boldsymbol{V_0}$ is calculated by minimizing equation (5), and then σ_1 is estimated through a Monte Carlo simulation. Since S^2 is a measure of dispersion, an initial estimate of σ_1^2 is taken to be S^2, and a set of simulations is performed where a new velocity is chosen for each WD at its position in the sky from the isothermal distribution with the assumed dispersion tensor and the calculated mean velocity. The error in tangential velocity, assumed to be Gaussian, is added to this. The set of simulations produces a distribution of S^2 values, and σ_1^2 is iterated until the mean S^2 corresponds to the value calculated from observations. S^2 is almost proportional to σ_1^2 when errors in tangential velocity are neglected and so the error in σ_1^2 is estimated from the distribution of S^2 scaled by this proportionality constant.

3.2 MCMC estimate

In addition, an MCMC likelihood-based estimate of the kinematic parameters was obtained. We use uninformative flat priors for the fitted parameters.

We denote the probability that the velocity of the ith object was $\boldsymbol{V}$ to be $P(\boldsymbol{V}|\boldsymbol{D}_i, \boldsymbol{\sigma}_i)$ where $\boldsymbol{D}_i = (l, b, d, \mu_\ell, \mu_\mathrm{b})$ is the data for the ith object together with the corresponding errors $\boldsymbol{\sigma}_i$. μ_ℓ and μ_b are the values corrected for galactic rotation by equation (2). Under the assumption that positions are uncorrelated with velocity, the distribution function is a function only of velocity: $f(\boldsymbol{V})$. In addition, in what follows we do not consider the positions, but instead focus on the kinematics through the velocity $\boldsymbol{V}$. Under these assumptions, the overall likelihood for a set of observations of a group of WDs is

$$\mathcal{L} = \prod_i \int \mathrm{d}\boldsymbol{V}\, f(\boldsymbol{V}) P(\boldsymbol{V}|\boldsymbol{D}_i, \boldsymbol{\sigma}_i) \tag{7}$$

$$\Rightarrow \log \mathcal{L} = \sum_i \log \int \mathrm{d}\boldsymbol{V}\, f(\boldsymbol{V}) P(\boldsymbol{V}|\boldsymbol{D}_i, \boldsymbol{\sigma}_i) \tag{8}$$

$$\equiv \sum_i \log \mathcal{L}_i\,. \tag{9}$$

In calculating the likelihoods, $\mathcal{L}_i$, we assume a Schwarzschild distribution function, and a normally distributed error in proper motion. The unknown radial velocity is integrated over analytically. Explicit expressions for $\mathcal{L}_i$ are given in Appendix A.

Again, the dispersion tensor and mean were constrained to reduce the number of parameters. We use flat priors on the dispersion and asymmetric drift. The expression for the likelihood was used to calculate the maximum likelihood estimate of the dispersion tensor, while errors were estimated from an MCMC using Metropolis–Hastings sampling. When the constraints on the dispersion tensor and mean velocity were relaxed this did not substantially alter the results, aside from the larger errors, particularly in the underpopulated bins due to the reduced degrees of freedom. In particular, the results are insensitive to allowing vertex deviation.

The fitting results for the SDSS and PG samples are summarized in Table 2 and plotted in Fig. 3. In addition, in Fig. 4 the raw transverse velocities measured from the proper motions for three groups of WDs are shown. The lowest mass WDs, $M < 0.45\,\mathrm{M}_\odot$, are expected to be predominantly formed through binary evolution and have a binary WD partner. This potentially introduces errors into their photometric distances and so we do not consider them beyond simply stating the fitting results in Table 2.

4 EXPECTATIONS FROM SSE

4.1 Analytic

In this section, we describe the reasons for the relationshipbetween WD mass and dispersion within a simple analytic model, before moving on to the more complex Monte Carlo simulations of Section 4.2.

Within the framework of SSE, an ensemble of WDs with the same mass would be expected to have a dispersion $\sigma(t_\mathrm{TOT})$, where $\sigma(t)$ is the disc-heating relation, and t_TOT is the total age of the WD including its precursor lifetime (i.e. total pre-WD stellar lifetime). Here, t_TOT will be given by $t_\mathrm{TOT} = t_\mathrm{WD} + t_\mathrm{SSE}(M_\mathrm{i}(M_\mathrm{WD}))$ where t_WD is the cooling age of the WD and $t_\mathrm{SSE}(M_\mathrm{i}(M_\mathrm{WD}))$ is the total precursor lifetime, which is a function of the WD mass through the initial–final mass relation (IFMR) $M_\mathrm{i}(M_\mathrm{f})$. Two components of this prediction are particularly uncertain: the disc-heating relation and the IFMR. We discuss these now.

The best constraints on the IFMR come from open clusters. Spectroscopic fits of the masses of WDs give the final mass. The initial mass is estimated using isochrone fitting to the main-sequence

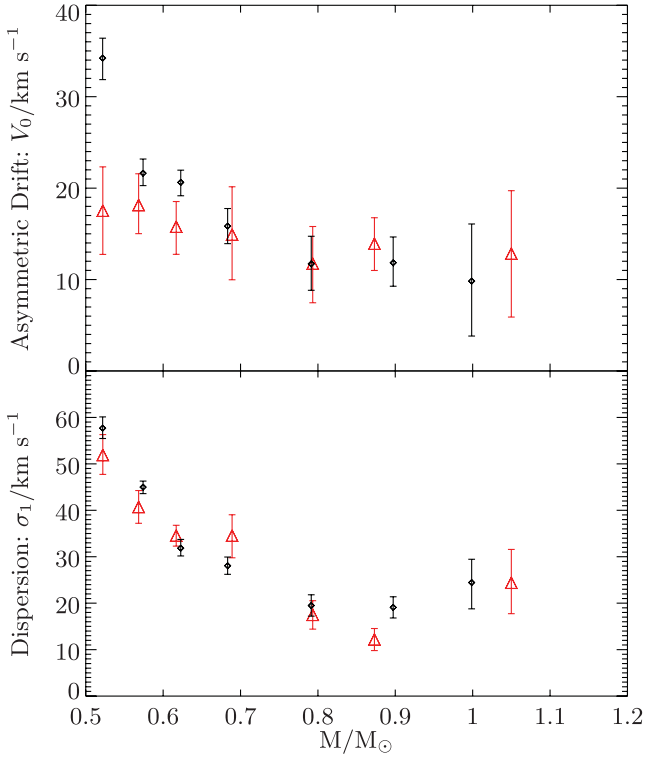

Figure 3. Dispersion of SDSS (black) and PG (red) WDs against mass calculated using the method described in Section 3.2. Each bin is plotted at its mean mass.

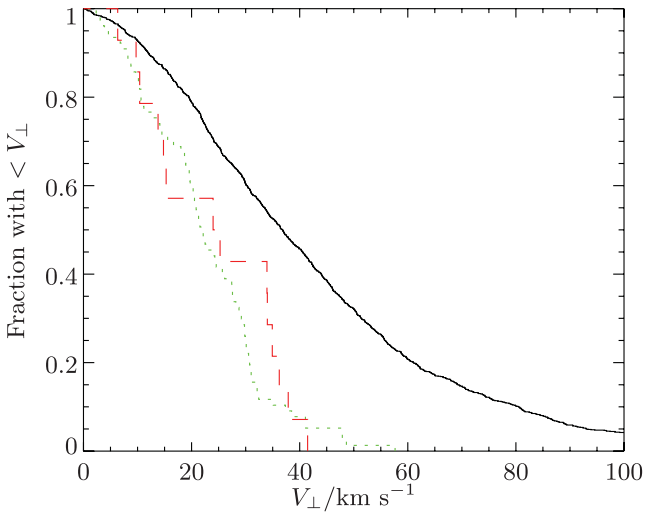

Figure 4. Cumulative transverse velocity distribution of the combined SDSS and PG surveys. Low-mass WDs ($0.5\,M_\odot \leq M < 0.75\,M_\odot$, with $M = M_1 + M_2$) as solid black, high-mass WDs ($M > 0.95\,M_\odot$) as dashed red and intermediate mass WDs ($0.75\,M_\odot \leq M < 0.95\,M_\odot$) as dotted green.

turnoff to calculate the age of the cluster, which finally allows the corresponding initial mass to be inferred using the precursor lifetime (Catalán et al. 2008). This method has succeeded in producing IFMRs with a typical uncertainty of less than 20 per cent. The strong dependance of the precursor lifetime on mass however makes this a considerable uncertainty in the dispersion relation.

The most accurate data on the disc-heating relation are given in Nordström et al. (2004) from an analysis of F and G dwarfs with

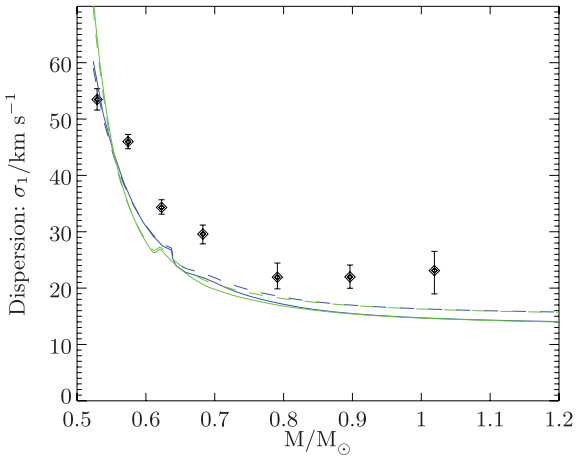

Figure 5. Predicted dispersions from models A–D, as dashed blue, solid blue, dashed green and solid green, respectively. Also plotted are SDSS WDs (black error bars) with the data taken from the MCMC column of Table 2.

radial velocities and *Hipparcos* data, although these data still permit a range of heating models (Seabroke & Gilmore 2007). However, for consistency, we instead use the disc-heating models estimated in Just & Jahreiß (2010), since we also use their companion star formation histories.

The effect of these model uncertainties are shown in Fig. 5 for the models described in Table 3. Qualitatively the results appear to agree with the predicted relations: for WDs more massive than $0.75\,M_\odot$, the WD progenitors' precursor lifetime is short and there is little dependence of the kinematics on mass. Below $0.75\,M_\odot$ the dispersion sharply increases as the progenitor lifetime approached 1 Gyr and longer where the disc heating is significant.

However, while qualitatively the results in Fig. 5 are consistent, there is quantitative disagreement. To assess this disagreement, we turn to a more sophisticated Monte Carlo treatment.

4.2 Monte Carlo

As a quantitative check of our results in Section 4.1, we have performed a Monte Carlo simulation of the production, kinematics and observation of the WDs in the solar neighbourhood, as described in this section. We also describe the simulated selection and observation of these WDs by the SDSS and PG. We perform this simulation to assuage fears that our results could be impacted by effects such as selection biases.

This process is somewhat involved, and so for clarity it is summarized in the flowcharts in Figs 6–8. The final results of the Monte Carlo simulation are compared with the WD sample in Fig. 10.

4.3 Picking stars

The initial mass was drawn from a Kroupa initial mass function (IMF) and one of two star-formation histories (Table 3). If this resulted in a WD at the present time with an age less than 3×10^8 yr, and a temperature between 13 000 and 40 000 K using the cooling models of Wood (1995) as explained in Section 2, then it was included in the simulation. See Fig. 6 for synopsis.

Table 3. Model input parameters for the models of SSE.

Model	$\sigma(t)$ (km s^{-1})	$M_{\rm i}(M_{\rm WD})$ (M$_\odot$)	$t_{\rm SSE}(M_{\rm i})$ (Gyr)	SFR(t)[a]
A	$66\left(\frac{0.5+t/\rm Gyr}{0.5+12}\right)^{1/2}$[b]	From Hurley, Pols & Tout (2000), solar metallicity		3.25[b]
B	$62\left(\frac{0.32+t/\rm Gyr}{0.32+10}\right)^{1/2}$[c]	From Hurley et al. (2000), solar metallicity		7.68 exp ($-t$/8 Gyr)[c]
C	$66\left(\frac{0.5+t/\rm Gyr}{0.5+12}\right)^{1/2}$[b]	From Catalán et al. (2008)	From Girardi et al. (2000)[b]	3.25[b]
D	$62\left(\frac{0.32+t/\rm Gyr}{0.32+12}\right)^{1/2}$[c]	From Catalán et al. (2008)	From Girardi et al. (2000)[c]	7.68 exp ($-t$/8 Gyr)[c]

[a]In units of M$_\odot$ pc^{-2} Gyr^{-1}. Not used in the analytic SSE simulation of Section 4.1. Star formation rate (SFR).
[b]Just & Jahreiß (2010) model C. Disc age 12 Gyr. Girardi et al. (2000) models use metal enrichment from Just & Jahreiß (2010) model C.
[c]Just & Jahreiß (2010) model D. Disc age 10 Gyr. Girardi et al. (2000) models use metal enrichment from Just & Jahreiß (2010) model D.

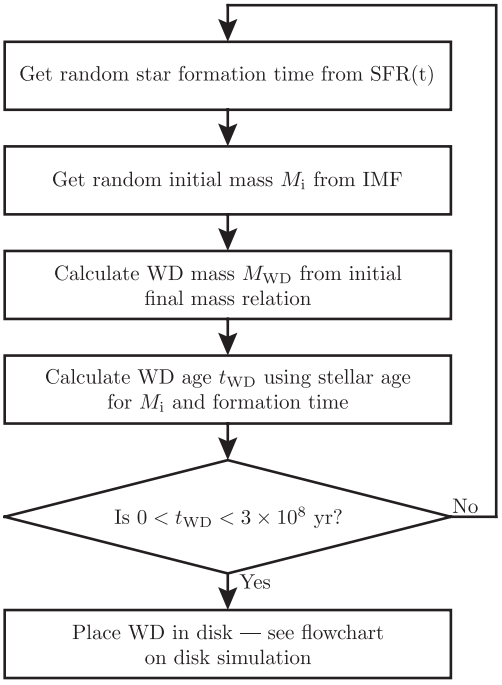

Figure 6. Flowchart illustrating the process of simulating WDs formed from SSE. If a star reaches the final stage, then it is placed in the disc using a process described by the flowchart shown in Fig. 7.

4.4 Placing stars in a disc

If a star has been included in the simulation, it is given a velocity dispersion taken from the previously described disc-heating models of Table 3 and axis ratios of the velocity ellipsoid of 1:1/1.4:1/2.2 (Dehnen & Binney 1998). Its velocity in the disc was drawn from a Gaussian with these widths and it was placed in the plane of the Galaxy using a radial exponential disc with a scale length of 2.5 kpc. Since the furthest $>0.47\,{\rm M}_\odot$ WD projected into the plane is less than 1 kpc, only WDs placed within this distance are simulated further.

For an isothermal population, the vertical position, z, and velocity, v_z, are given by

$$f_z(E_z) \propto \exp\left(-E_z/\sigma_z^2\right) \propto \exp\left(-v_z^2/2\sigma_z^2\right)\exp\left(-\Phi_z(z)/\sigma_z^2\right), \quad (10)$$

where Φ_z is the gravitational potential. Each star's velocity is thus drawn from a Gaussian with standard deviation given by the

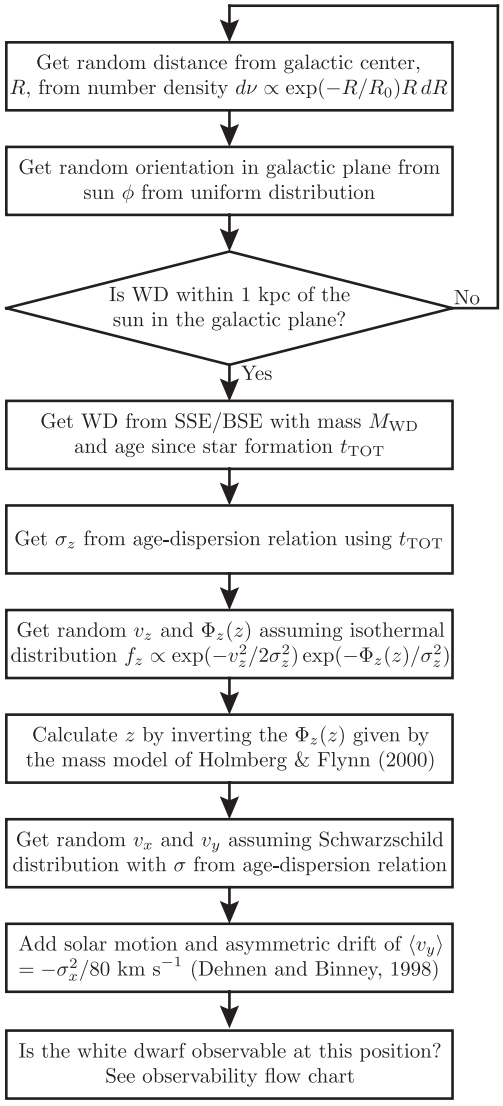

Figure 7. Flowchart illustrating the process of placing WDs in the galactic disc and picking their velocity. This process is undertaken if a star reaches the final stage of the flowchart shown in Fig. 7. If a star reaches the final stage of this flowchart, the observability is finally determined using the algorithm described in the flowchart shown in Fig. 8.

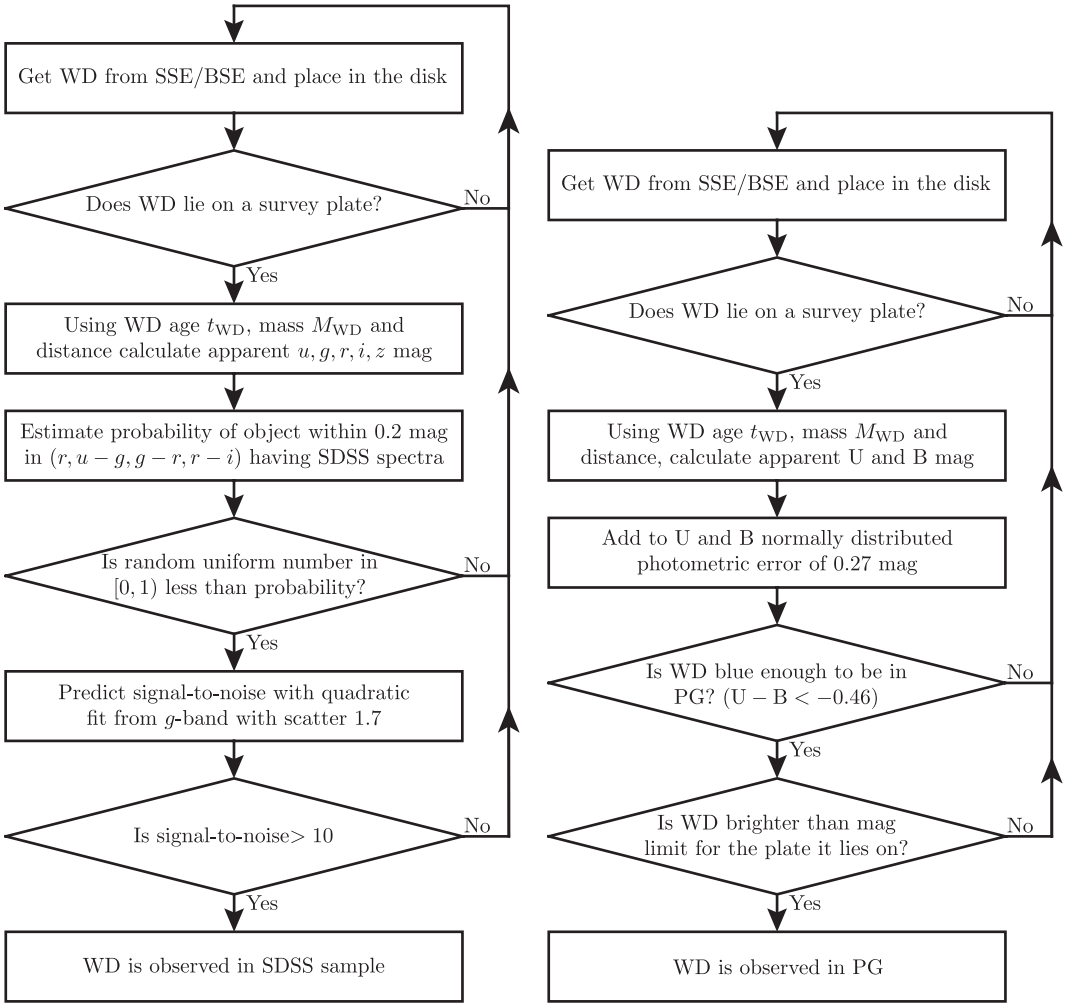

Figure 8. Flowchart illustrating the process of simulating whether WDs are observed. This process is undertaken if a star has reached the final stage of the flowchart shown in Fig. 7.

previously calculated σ_z, while z is chosen by first drawing $\Phi_z(z)$ from an exponential distribution with scale σ_z^2, and then inverting this to calculate z. We use the mass models of Holmberg & Flynn (2000) for $\Phi_z(z)$.

This process of placing WDs in the local galactic disc is summarized in Fig. 7.

4.5 WD observability

As a result of this process, each WD has an assigned galactic position and velocity, together with its mass and age. It is then assessed whether it is likely to be observed in either the SDSS or PG survey as follows. First its galactic position is translated to a right ascension, RA, and declination, Dec., and, unless this falls on one of the PG plates or the SDSS DR4 spectroscopic plates, the probability of observation is zero.

For WDs in the PG survey, the apparent U and B magnitudes are calculated from the models of Holberg & Bergeron (2006) with a 0.27 mag error added to each to mimic the photometric errors in PG (Liebert et al. 2005). If it is bluer than $U - B = -0.46$ and brighter than the B-band magnitude limit for the PG plate on which it lies, then it is considered observed.

For the SDSS, the spectroscopic targeting is more complex (Kleinman et al. 2004), and the strategy was to construct an empirical observational probability for a star at each magnitude and colour. A four-dimensional table of probability of spectroscopic follow-up was constructed in $(r, u-g, g-r, r-i)$ grouped in 0.2 mag bins from the SDSS DR4 clean photometry. The expected spectroscopic signal-to-noise was calculated using a quadratic least-squares fit to the observed signal-to-noise ratio as a function of g-band magnitude together with normally distributed scatter in signal-to-noise with a standard deviation of 1.7. If the signal-to-noise ratio was greater than 10, it was included in the mock sample.

Finally, measurement errors in the mass of 0.03 $M_\odot$ and proper motion errors of 5.6 mas yr^{-1} are introduced.

The process of assessing if each WD is observed by the PG survey or SDSS is summarized in Fig. 8. In all simulations, we simulate a total of $\sim 2 \times 10^{11}$ objects.

4.6 Monte Carlo results

The results of this simulation are shown in Fig. 10. As a further check that the simulated WDs have the correct kinematics, we plot the distributions in the U, V and W directions (directed towards the

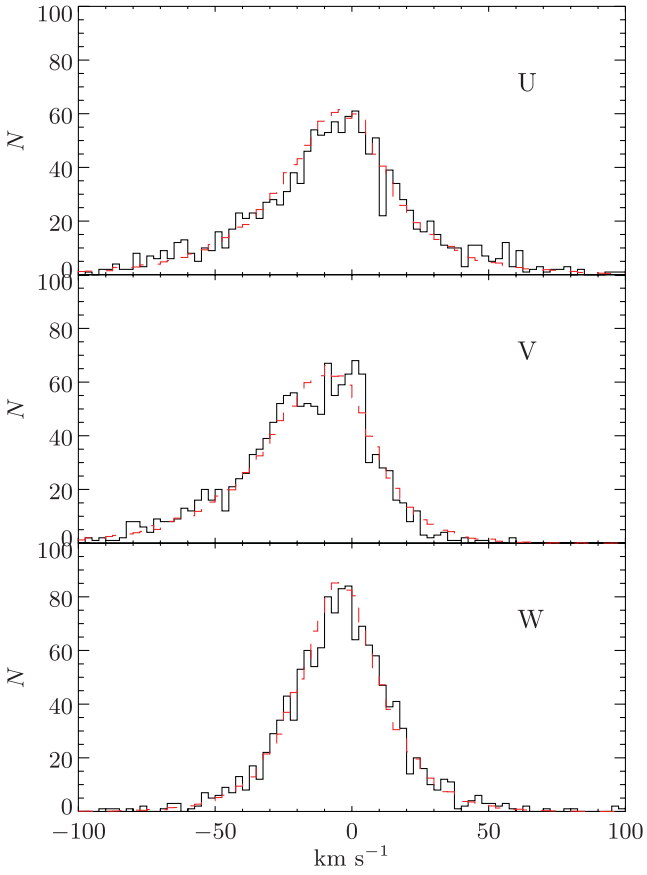

Figure 9. Histograms showing the agreement between the observed and simulated velocity distribution in the U, V, W directions of SDSS WDs. The black line is the observed distribution, while the dashed red line is the distribution of the SSE simulation for model C. Zero radial velocity is artificially assumed, and the number of simulated WDs is normalized to the number observed. U is directed towards the galactic centre, V in the direction of galactic rotation and W towards the north Galactic pole.

galactic centre, in the direction of galactic rotation and towards the north Galactic pole, respectively) in Fig. 9.

The results of the SSE simulation, described in this section, closely agree with the observations, modulo the normalization factor. We do not concern ourselves with this overall normalization; however, the normalization factor is typically $\lesssim 2$. The simulation also does not produce WDs below $\approx 0.47\,\mathrm{M}_\odot$, which are generally expected to form through binary evolution. As may be expected from the analytic models plotted in Fig. 5, the models in Table 3 all produce WDs that reasonably closely explain the observed samples and their kinematics and so we only plot the results of only one representative model in Fig. 10.

5 EXPECTATIONS FROM BINARY STAR EVOLUTION

It has been suggested that the majority of high-mass WDs were formed from mergers of binary WDs, both on the basis of their number density (Liebert et al. 2005) and a possible peak at $1\,\mathrm{M}_\odot$ (Vennes 1999). To test this hypothesis, we use two binary evolution codes (discussed in Section 5.1) to perform binary population synthesis (described in Section 5.2), and ultimately what fraction of the sample is likely to have had a binary WD progenitor (Section 5.3).

5.1 Binary evolution codes

To address the considerable uncertainties in binary evolution, two binary evolution codes were used. Specifically, the `BSE` code described in Hurley et al. (2000), and the `SeBa` code described in Nelemans et al. (2001). Both codes use the same approach to modelling binary evolution: semi-analytic fits to the structure and evolution of isolated stars are combined with prescriptions for interactions between the stars.

There are four key initial conditions that govern the evolution of a binary: the initial primary mass $M_{1\mathrm{i}}$, the initial secondary mass $M_{2\mathrm{i}}$ (or equivalently the mass ratio $q_\mathrm{i} = M_{1\mathrm{i}}/M_{2\mathrm{i}}$), the initial binary semi-major axis a_i and the initial eccentricity e_i.

One slice through the four-dimensional space of initial conditions $(M_{1\mathrm{i}}, q_\mathrm{i}, a_\mathrm{i}, e_\mathrm{i})$ showing those conditions which result in the merger of a pair of WDs is shown in Fig. 11.

The differences between the `BSE` code and the `SeBa` code in Fig. 11 are striking, and are largely due to the different binary evolution prescriptions, and in particular the treatment of the Roche lobe overflow (RLOF) and common envelope (CE) phases.

For the specifics of the treatment of the RLOF phase and its treatment in the `BSE` and `SeBa` codes, we refer the reader to Hurley et al. (2000) and Nelemans et al. (2001), respectively. There is also considerable uncertainty in the treatment of the important CE evolution phase. The most fundamental difference between the codes is the treatment of the first phase of mass transfer. `BSE` uses the most commonly used prescription for the CE evolution known as the α parametrization for both phases of mass transfer. `SeBa`, however, by default uses the γ parametrization. We refer the reader to Nelemans et al. (2001) for the details of these parameterisations.

To assess the result of the considerable uncertainties in binary evolution on the merger time distribution, and therefore the resultant velocity distributions, we have used four models across the two binary evolution codes. These models are summarized in Table 4.

5.2 Binary population synthesis

We now describe our method of binary population synthesis.

We use the same distributions in the parameters $(M_{1\mathrm{i}}, q_\mathrm{i}, a_\mathrm{i}, e_\mathrm{i})$ as Han (1998) and Nelemans et al. (2001) with the exception of the IMF for which we use a Kroupa (2001) IMF as opposed to a Miller & Scalo (1979) IMF. For reference, the probability distributions are

$$\begin{aligned} P(M_{1\mathrm{i}}) &\propto M_{1\mathrm{i}}^{-1.35} \quad & 0.8 < M_{1\mathrm{i}} \leq 10\,, \\ P(q_\mathrm{i}) &\propto \text{const.} \quad & 0 < q \leq 1\,, \\ P(\log a_\mathrm{i}) &\propto \text{const.} \quad & 0 < \log a_\mathrm{i}/\,\mathrm{R}_\odot \leq 5\,, \\ P(e_\mathrm{i}) &\propto e_\mathrm{i} \quad & 0 \leq e_\mathrm{i} < 1\,. \end{aligned} \tag{11}$$

Our approach to simulating the results of BSE is to first produce a four-dimensional grid of binary simulations in the parameters $(M_{1\mathrm{i}}, q_\mathrm{i}, a_\mathrm{i}, e_\mathrm{i})$. Grid points were linearly spaced in $M_{1\mathrm{i}}$ between 0.8 and $10\,\mathrm{M}_\odot$, linearly spaced in q_i between 0 and 1, logarithmically spaced in a_i between 1 and $10^4\,\mathrm{R}_\odot$, and linearly spaced in e_i^2 between 0 and 1. The grid size used was a $25 \times 25 \times 50 \times 10$ grid in $(M_{1\mathrm{i}}, q_\mathrm{i}, a_\mathrm{i}, e_\mathrm{i})$, respectively. With this choice of grid combined with the distributions in equation (11), the population synthesis is particularly simple: an initial primary mass is drawn from the Kroupa (2001) IMF and a random binary from the closest corresponding $(q_\mathrm{i}, a_\mathrm{i}, e_\mathrm{i})$ slice is chosen. In all simulations, a total of $\sim 10^{13}$ objects are placed in the disc.

The process of simulating stars formed from binary evolution is summarized in Fig. 12.

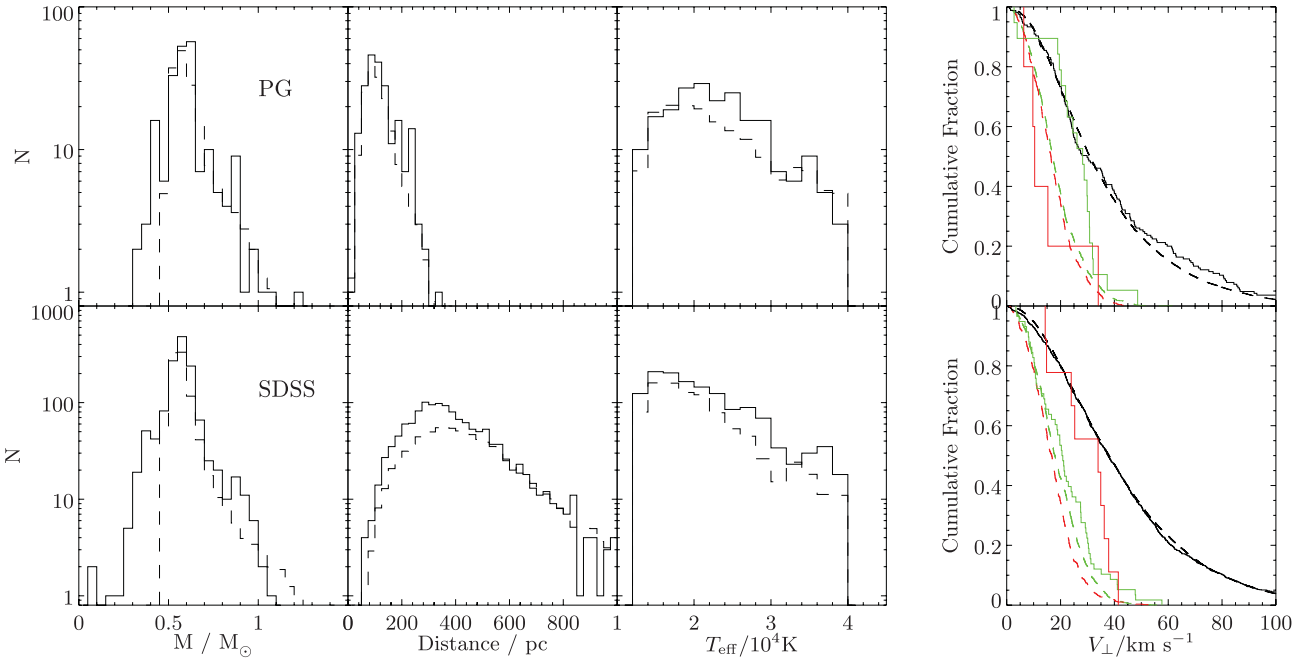

Figure 10. Comparison between the observed WDs as the solid lines, and the Monte Carlo simulations of SSE described in Section 4.2 as the dashed lines. The upper panels show the PG survey and the lower panels the SDSS. The rightmost panel shows the cumulative transverse velocity distribution. In this panel, colours are as in Fig. 4. Specifically low-mass WDs ($0.5\,{\rm M}_\odot \leq M_1 + M_2 < 0.75\,{\rm M}_\odot$) are plotted in black, high-mass ($M_1 + M_2 > 0.95\,{\rm M}_\odot$) WDs in red and intermediate-mass WDs ($0.75\,{\rm M}_\odot \leq M_1 + M_2 < 0.95\,{\rm M}_\odot$) in green. The simulation plotted is model D from Table 3.

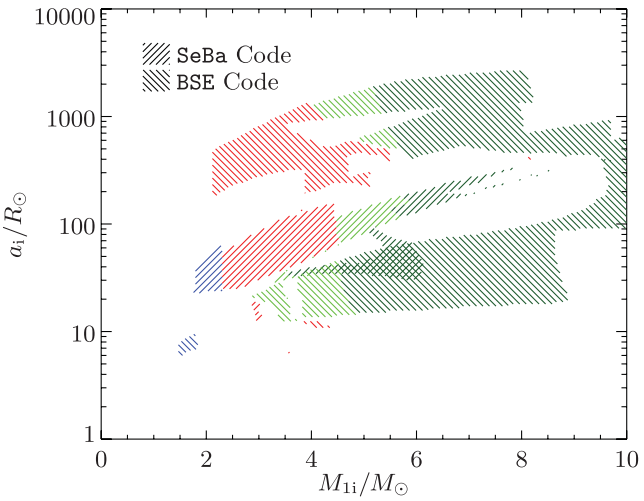

Figure 11. Comparison of the WD+WD merger outcomes from the SeBa and BSE codes with their default prescriptions for binary evolution. All simulations use an initial mass ratio of $q_{\rm i} = 0.5$ and eccentricity of $e_{\rm i} = 0$. Green corresponds to CO+CO, red He+CO and blue He+He. The light green are sub-Chandrasekhar ($M_1 + M_2 < 1.4\,{\rm M}_\odot$) mergers, and the darker green super-Chandrasekhar.

Table 4. Summary of the four binary evolution models considered. The BSE code is that described by Hurley et al. (2000), and the SeBa code is described in Nelemans et al. (2001). The CE prescription describes how the two phases of CE evolution are treated. For example, $\gamma\alpha$ describes the treatment of the first phase through the γ parametrization and the second through the α parametrization. We refer the reader to Nelemans et al. (2001) for the definition and descriptions of these parametrizations.

Model	Evolution code	CE prescription	$\alpha_{\rm CE}\lambda$	γ
i	BSE	$\alpha\alpha$	2	–
ii	BSE	$\alpha\alpha$	1	–
iii	SeBa	$\gamma\alpha$	2	1.5
iv	SeBa	$\alpha\alpha$	2	–

In what follows, we concern ourselves with the merger of CO+CO WDs, since these are the mergers proposed to the result in $\gtrsim$1 M$_\odot$ WDs. Thus, in Fig. 13, we plot the rate at which pairs of WDs with sub-Chandrasekhar total mass merge as calculated from our binary population synthesis of the four models in Table 4. Note that the overall normalization can be very different. In particular, model ii uses a relatively efficient CE prescription with $\alpha_{\rm CE}\lambda = 1$ for both phases of mass transfer. This in turn results in a smaller range of initial separations that will ultimately result in a gravitational radiation-driven WD merger. Despite the differences in the overall rate between the models, they all display a similar *distribution* of merger times. This is because, apart from at early times, the merger time is dominated by the time to merge by gravitational radiation. This is a strong function of separation, a, specifically $t_{\rm GW} \propto a^4$. As a result, at late times, the merging WDs originally formed a narrow range in separation at WD+WD birth. Approximating this as a power law, $\frac{{\rm d}N}{{\rm d}a} \propto a^\epsilon$ leads to a merger rate $\frac{{\rm d}N}{{\rm d}t} = \frac{{\rm d}N}{{\rm d}a}\frac{{\rm d}a}{{\rm d}t} \propto t^{-(3-\epsilon)/4}$, and so for a wide range of ϵ the merger rate declines as $\frac{{\rm d}N}{{\rm d}t} \sim t^{-1}$ (Maoz, Sharon & Gal-Yam 2010).

5.3 Proportion of high-mass white dwarfs formed in mergers

To assess the possible proportion of high-mass WDs that formed through mergers, the CO+CO merger products with

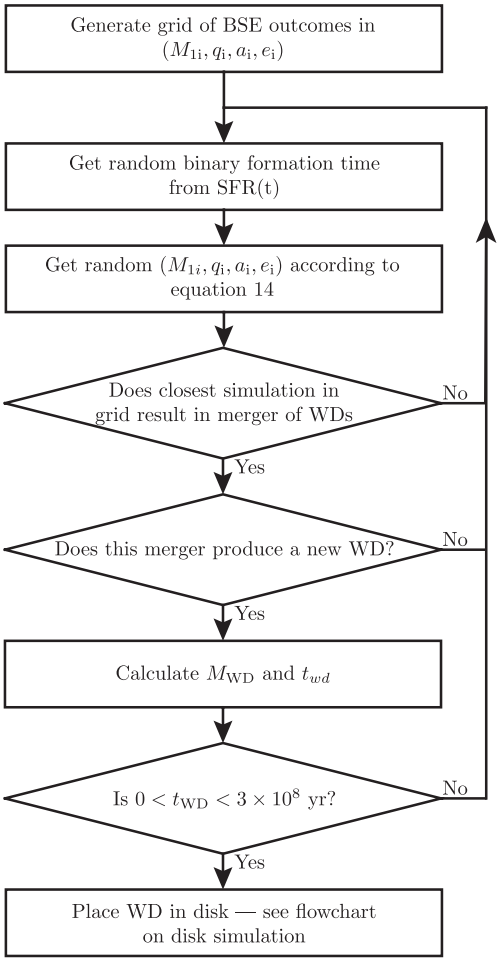

Figure 12. Flowchart illustrating the process of simulating WDs formed from binary star evolution (BSE).

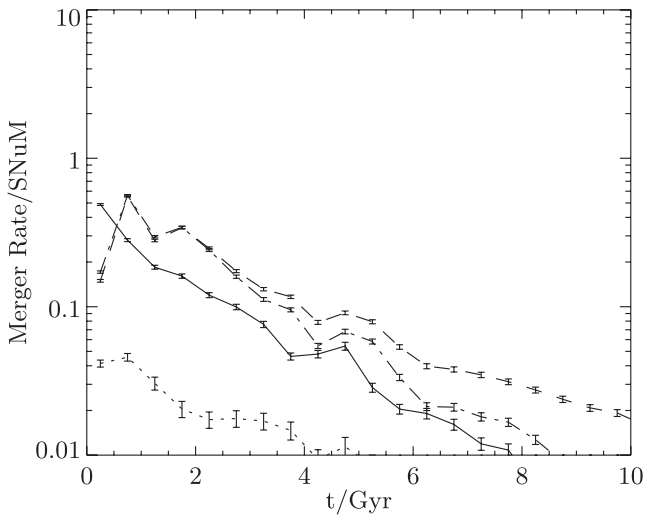

Figure 13. Merger rates of CO+CO WDs with sub-Chandrasekhar total mass following a burst of star formation. The error bars are purely statistical due to the finite size of the simulated binary grid. Lines are models i–iv as solid line, dotted line, dashed line and dash–dotted line, respectively. The models are described in Table 4. SNuM $\equiv 1/(100\ \mathrm{yr})/(10^{10}\mathrm{M}_\odot)$.

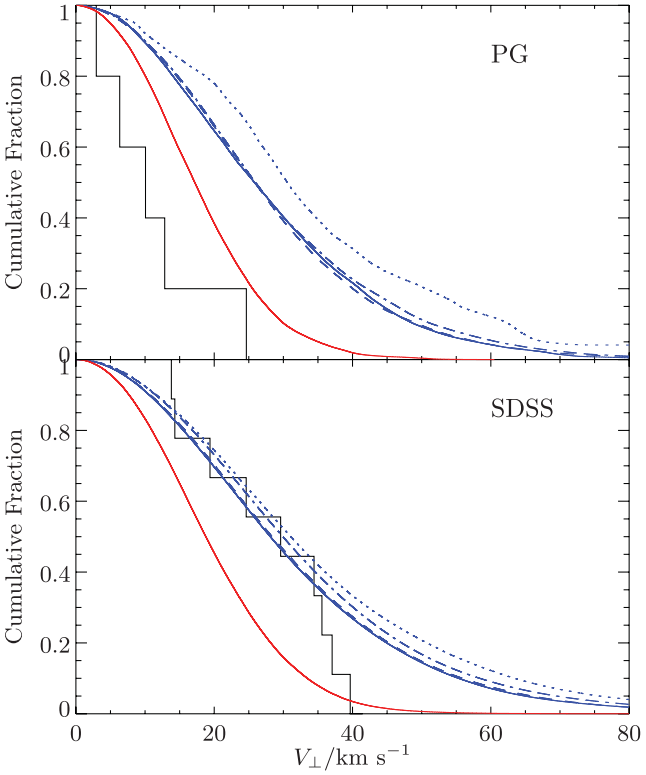

Figure 14. Predicted distribution of transverse velocities observed in SDSS and PG resulting from the merger of CO+CO WDs with $0.95 < M_1 + M_2/\mathrm{M}_\odot < 1.4$. Lines are the `BSE` code with $\alpha_{\mathrm{CE}}\lambda = 2$ (solid blue line, model i), the `BSE` code with $\alpha_{\mathrm{CE}}\lambda = 1$ (dotted blue line, model ii), the `SeBa` code using the $\gamma\alpha$ CE prescription (dashed blue line, model iii) and the `SeBa` code using the $\alpha\alpha$ prescription (dash–dotted blue line, model iv). Both `SeBa` models use $\alpha_{\mathrm{CE}}\lambda = 2$ and $\gamma = 1.5$. The red line is the predicted distribution of transverse velocities resulting from SSE to a $0.95 < M/\mathrm{M}_\odot < 1.4$ WD according to model A in Table 3, and the black lines are the observed distributions. All BSE models use a constant SFR and the disc-heating relation of model A in Table 3.

$0.95\,\mathrm{M}_\odot \leq M_1 + M_2 < 1.4\,\mathrm{M}_\odot$ from the binary population synthesis are subjected to the same process as the single population synthesis results, i.e. they are placed locally in the disc according to the method summarized in Fig. 7 and their observability in the SDSS and PG samples assessed according to Fig. 8.

We assume that no mass is ejected during the merger so that the resultant WD has mass $M_{\mathrm{WD}} = M_1 + M_2$. We also assume that the merger reheats the WD sufficiently that the WD has a cooling age of

$$t_{\mathrm{WD}} = t_{\mathrm{form}} - t_{\mathrm{merge}},$$

where t_{form} is the time prior to the present at which the binary initially formed, and t_{merge} is the length of time it took for the merger to occur, including the precursor lifetime. The resulting cumulative transverse velocity of $0.95\,\mathrm{M}_\odot \leq M_1 + M_2 < 1.4\,\mathrm{M}_\odot$ CO+CO merger products is shown in Fig. 14.

In Fig. 14 and the following, we have combined the PG and SDSS samples to improve the statistics. We combine the Monte Carlo results by the empirical proportions of WDs in this sample, i.e. the observed PG to SDSS ratio of 5:9. Note however that there is a possible discrepancy between the two samples in this high mass bin. In particular, the SDSS sample has few low velocity ($<14\,\mathrm{km\,s^{-1}}$) WDs (see the bottom-right panel of Fig. 10), and this results in a 12 per cent probability that they are drawn from the same distribution.

The distribution of transverse velocities in Fig. 14 shows that despite the uncertainties in binary evolution resulting in very different binary histories (Fig. 11) and overall merger rates (Fig. 13), the resultant velocity distributions are very similar. This is a result of the $\sim t^{-1}$ merger time distribution at late times discussed previously.

The results in Fig. 14 naturally lead to the question of what fraction of mergers is consistent with the data to be addressed. We wish to assess the fraction of high-mass galactic WDs formed by binary mergers (BSE) which we parametrize by θ. This results in a fraction $1-\theta$ from SSE. To assess a value of θ for a given SSE and BSE Monte Carlo realization, we first calculate the galactic formation rate of high-mass WDs from SSE and BSE in this realization, which we denote $\Gamma_{\rm SSE}$ and $\Gamma_{\rm BSE}$, respectively. Then, for both PG and SDSS we make α copies of the BSE objects simulated as observed, and β copies of objects simulated as observed from SSE. Assuming that equal numbers of objects were simulated in both the BSE and SSE realizations, the two simulated samples combined have a galactic BSE fraction of

$$\theta = \frac{\beta\Gamma_{\rm BSE}}{\beta\Gamma_{\rm BSE} + \alpha\Gamma_{\rm SSE}} .$$

To test whether the data are consistent with this realization, we use the two-sample Anderson–Darling statistic (Pettitt 1976). The Anderson–Darling test considers the difference between the samples across the entire distribution, and so is more statistically powerful than the more commonly used Kolmogorov–Smirnov test which depends only on the extremum. The number of simulated WDs is always much larger, by at least a factor of 10, than the number observed.

The results for one particular choice of SSE and BSE models are shown in Fig. 15(a). In Fig. 15(b), we show the combined probability that the PG and SDSS samples are consistent with each value of θ. In Table 5, we summarize the results of this procedure for the range of the BSE and SSE models described in tables 3 and 4.

The results in Table 5 show that for the majority of models the fiducial numbers of WDs formed via SSE and BSE are consistent with the data. The results taken at face value would also appear to show that, for most models, at the 1 per cent probability level, high-mass WDs must come from a combination of SSE and mergers of high-mass WDs. This appears artificial however: from the right-hand column of Fig. 15(a), the PG sample is consistent with all SSE, while the SDSS sample that has a low probability of arising purely from SSE.

This is a result of the lack of low velocity ($<14\,{\rm km\,s^{-1}}$) WDs in the SDSS sample. It may be that the lack of low velocity WDs in SDSS is a statistical anomaly, since the number of objects is small. In theory, this would be taken account of in the analysis described above; however, young stellar objects can display a prominent substructure in their kinematics as a result of moving groups (e.g. Dehnen 1998). This would have the result of both reducing the effective sample size and producing a very different velocity distribution than the Schwarzschild distribution assumed in the SSE Monte Carlo. There are indications that this is the case, since when the SDSS objects are plotted in the $U-V$ plane (assuming zero radial velocity), seven of the nine objects lie in the negative U, negative V quadrant. Depending on the unobserved radial velocity, many of these could have kinematics consistent with the Pleiades and Hyades moving groups. Indeed it has been shown that the WD GD 50 has a velocity and cooling age consistent with a Pleiades origin (Dobbie et al. 2006).

That the data rule out a WD merger origin for the majority of high-mass WDs appears more secure, despite the apparent consistency of the SDSS sample with the BSE simulations: the PG sample is entirely consistent with SSE, and neither sample contains a high-mass WD travelling at $>50\,{\rm km\,s^{-1}}$ which would be convincing evidence of a BSE origin for some high-mass WDs. This is not surprising, since the expected number of merger products observed in PG and SDSS ($N_{\rm BSE}$ in Table 5) is significantly smaller than the observed number of objects.

We note that a simpler empirical test for the origin of the high-mass WDs is suggested by Fig. 4. The distribution of high-mass WDs is consistent with the velocity distribution of the intermediate

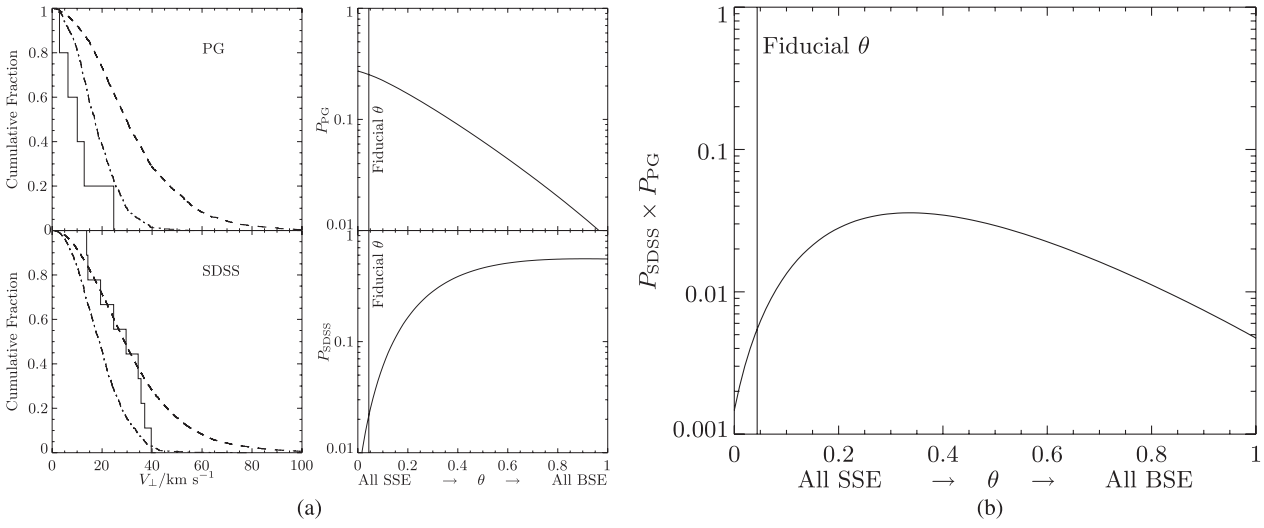

Figure 15. Plots showing the calculation of the galactic formation fraction of high-mass WDs formed in mergers during BSE in model C compared to SSE model iii. (a) The left-hand column shows the cumulative distribution of transverse velocities of high-mass ($M > 0.95\,{\rm M}_\odot$) WDs in the SDSS and PG survey. The dashed–dot lines are the predictions of the SSE model C and the dashed lines are the predictions of the BSE model iv. The right-hand column shows, for each fractional galactic formation fraction from BSE, θ, the probability that the velocity distribution is consistent with the data using the Anderson–Darling statistic for the PG sample, $P_{\rm PG}$, and the SDSS sample, $P_{\rm SDSS}$. The fiducial θ is the fiducial predicted galactic fraction from BSE model iii compared to SSE model C with 50 per cent binary fraction. (b) The combined probability that each value θ is consistent with both the PG and SDSS samples. Calculated by the product of the probabilities in the right-hand column of Fig. 15(a).

Table 5. Summary of the results of calculation of the fraction of high-mass WDs formed in mergers compared to SSE. The SSE models are described in Table 3 and the BSE models are described in Table 4. $\Gamma_{\rm BSE}$ is the galactic formation rate (in $\rm yr^{-1}$) from BSE assuming that the merger of two CO WDs with combined mass between 0.95 and 1.4 $\rm M_\odot$ results in a high-mass WD. $\Gamma_{\rm SSE}$ is the galactic formation rate from SSE. θ is the galactic fraction of high-mass WDs formed from BSE so that the fiducial value is given by $\theta_{\rm fid} \equiv \frac{\Gamma_{\rm SSE}}{\Gamma_{\rm BSE}+\Gamma_{\rm SSE}}$. The numbers $N_{\rm SSE}$ and $N_{\rm BSE}$ are the predicted observed numbers from SSE and BSE evolution, respectively, in the PG and SDSS samples. $P(\theta_{\rm fid})$ is the probability that *both* the PG and SDSS velocity distributions are consistent with $\theta_{\rm fid}$ using the Anderson–Darling statistic. $\theta(P > 0.05)$ is the range of θ values which have a probability of being consistent with the data greater than 1 per cent. The fiducial value of θ is calculated assuming a 50 per cent binary fraction (i.e. two-thirds of all stars formed in binaries). Both SSE and BSE models use the same disc-heating model and star formation history: model C of Table 3 for the constant SFR models, and model D for the exponential.

SFR	SSE model	BSE model	$\Gamma_{\rm BSE}$	$\Gamma_{\rm SSE}$	$\theta_{\rm fid}$	PG		SDSS		$P(\theta_{\rm fid})$	$\theta(P > 0.01)$
						$N_{\rm SSE}$	$N_{\rm BSE}$	$N_{\rm SSE}$	$N_{\rm BSE}$		
Const	C	i	0.0006	0.03	0.02	7	0.1	17	0.9	0.02	0.09–0.9
	C	ii	0.0001	0.03	0.005	7	0.02	17	0.1	0.005	0.08–0.8
	C	iii	0.001	0.03	0.04	7	0.3	17	2.0	0.04	0.08–0.8
	C	iv	0.001	0.03	0.04	7	0.3	17	2.0	0.04	0.09–1.0
Exp	D	i	0.0007	0.02	0.04	6	0.1	13	1.0	0.04	0.1–0.9
	D	ii	0.0002	0.02	0.01	6	0.02	13	0.2	0.01	0.2–0.8
	D	iii	0.001	0.02	0.07	6	0.3	13	3.0	0.07	0.1–0.9
	D	iv	0.001	0.02	0.06	6	0.3	13	2.0	0.06	0.2–0.9

group that displays the kinematics of young objects at the 13 per cent level by the Anderson–Darling test. This ignores the selection effects which the Monte Carlo simulation addresses, but does suggest that the entire combined group of high-mass WDs is broadly consistent with SSE.

6 SCALE HEIGHTS

One of the key results of this study is that hot WDs of mass $\gtrsim$0.75 $\rm M_\odot$ had much shorter main sequence lifetimes than their lower mass counterparts, and hence their kinematics are characteristic of young stars. A direct result of this is that these higher mass WDs will have reduced scale height. This is vitally important to consider when calculating the formation rate as a function of mass using local samples such as in Liebert et al. (2005) or Kepler et al. (2007) or producing galactic WD simulations such as Nelemans et al. (2001).

Unfortunately, neither the SDSS nor the PG sample allows accurate direct determination of the scale height of each WD population, particularly the rare and less luminous high-mass groups. Instead, here we list the expected scale height by comparison with the SSE models that appear to accurately describe the kinematics. We do this to allow simple initial corrections without resorting to the simulations of the type performed in this work. The scale height, h, was defined through

$$\nu(z) = \nu_0 \,\mathrm{sech}^2\left(\frac{z}{2h}\right), \tag{12}$$

where $\nu(z)$ is the stellar number density in terms of the height above the plane of the galactic disc, z. The scale height, h, was estimated by constraining equation (12) to give both the correct overall number and central WD density, ν_0. We choose this method since the most common usage of the scale height is to calculate galactic birthrates from local densities. The results are give in Table 6. Note that the higher mass groups smaller scale height results in a local density enhanced by more than a factor of 2 over the more common low-mass group. In particular, the apparent excess of high-mass WDs found in the PG survey (discussed in section 6 of Liebert et al. 2005) can be naturally explained by their lower scale height, which causes a high abundance in this relatively local survey. That the number of high-mass WDs is consistent with single star expectations in PG is confirmed by the number of expected WDs from SSE in Table 5.

Table 6. Scale heights, h, defined through equation (12) for three different mass groups. h is calculated by matching the central density and overall number to the simulations described in Section 4.2.

$M_{\rm low}$ ($\rm M_\odot$)	$M_{\rm high}$ ($\rm M_\odot$)	h (pc)
0.45	0.75	120
0.75	0.95	58
0.95	1.40	54

7 SUMMARY

We have analysed the kinematics of young ($<3 \times 10^8$ yr) DA WDs from both the PG survey and the SDSS and find a strong connection between their mass and kinematics: low-mass WDs ($0.45\,\rm M_\odot \leq M_1 + M_2 < 0.75\,M_\odot$) display the kinematics of old stars, with higher velocity dispersion ($\sim$46 $\rm km\,s^{-1}$) and asymmetric drift, while higher mass WDs ($0.75\,\rm M_\odot \leq M_1 + M_2 < 0.95\,M_\odot$) display the kinematics of young stars with a velocity dispersion of only $\sim$19 $\rm km\,s^{-1}$. We have shown in Section 4 that this is expected due to the shorter precursor lifetime of the more massive progenitors, and that there is agreement both on simple analytic grounds (Section 4.1) and more quantitative Monte Carlo simulations of the PG and SDSS samples (Section 4.2).

A further key conclusion is that the WD scale height and its variation with age and mass are vitally important to consider when calculating birth rates based on local samples (Section 6).

In addition, we have separately analysed the highest mass WDs ($M > 0.95\,\rm M_\odot$, Section 5), since it has been suggested that many of these formed as a result of the merger of two lower mass CO WDs. We find at present a discrepancy in the SDSS velocity distribution where no high-mass WDs with transverse velocity less than 14 $\rm km\,s^{-1}$ is detected. This results in a velocity distribution that within our statistical framework is inconsistent with purely SSE. We argue that this is likely to an anomaly, either be a statistical or a result of a number of these WDs being members of moving groups. We find that, even under the most optimistic binary evolution models, we would only expect to find three WDs formed via WD binary mergers and that the apparent excess of high-mass WDs found in PG is caused by their reduced scale height. In addition, we note the kinematic 'smoking gun' of some fraction of high-mass WDs

coming from binary evolution would be high-mass WDs travelling at $>50\,\mathrm{km\,s^{-1}}$, of which none are found in PG or SDSS.

ACKNOWLEDGMENTS

CW gratefully acknowledges many useful discussions with Nate Bode. Support for this work was provided by NASA BEFS grant NNX-07AH06G.

REFERENCES

Anselowitz T., Wasatonic R., Matthews K., Sion E. M., McCook G. P., 1999, PASP, 111, 702
Bergeron P. et al., 2011, ApJ, 737, 28
Catalán S., Isern J., García-Berro E., Ribas I., 2008, MNRAS, 387, 1693
Dehnen W., 1998, AJ, 115, 2384
Dehnen W., Binney J., 1998, MNRAS, 298, 387
Dobbie P., Napiwotzki R., Lodieu N., Burleigh M., Barstow M., Jameson R., 2006, MNRAS, 373, L45
Eisenstein D. J. et al., 2006, ApJS, 167, 40
Feast M., Whitelock P., 1997, MNRAS, 291, 683
Fontaine G., Brassard P., Bergeron P., 2001, PASP, 113, 409
Girardi L., Bressan A., Bertelli G., Chiosi C., 2000, A&AS, 141, 371
Guseinov O. K., Novruzova K. I., Rustamov I. S., 1983, Ap&SS, 97, 305
Han Z., 1998, MNRAS, 296, 1019
Holberg J. B., Bergeron P., 2006, AJ, 132, 1221
Holmberg J., Flynn C., 2000, MNRAS, 313, 209
Hurley J. R., Pols O. R., Tout C. A., 2000, MNRAS, 315, 543
Just A., Jahreiß H., 2010, MNRAS, 402, 461
Kepler S. O., Kleinman S. J., Nitta A., Koester D., Castanheira B. G., Giovannini O., Costa A. F. M., Althaus L. G., 2007, MNRAS, 375, 1315
Kleinman S. J. et al., 2004, ApJ, 607, 426
Kowalski P. M., Saumon D., 2006, ApJ, 651, L137
Kroupa P., 2001, MNRAS, 322, 231
Liebert J., Bergeron P., Holberg J. B., 2005, ApJS, 156, 47
Maoz D., Sharon K., Gal-Yam A., 2010, ApJ, 722, 1879
Miller G. E., Scalo J. M., 1979, ApJS, 41, 513
Munn J. A. et al., 2004, AJ, 127, 3034
Munn J. A. et al., 2008, AJ, 136, 895
Nelemans G., Yungelson L. R., Zwart S. F. P., Verbunt F., 2001, A&A, 365, 491
Nordström B. et al., 2004, A&A, 418, 989
Oppenheimer B. R., Hambly N. C., Digby A. P., Hodgkin S. T., Saumon D., 2001, Sci, 292, 698
Pauli E.-M., Napiwotzki R., Heber U., Altmann M., Odenkirchen M., 2006, A&A, 447, 173
Pettitt A., 1976, Biometrika, 63, 161
Ratnatunga K. U., Bahcall J. N., Casertano S., 1989, ApJ, 339, 106
Reid I. N., 2005, ARA&A, 43, 247
Roeser S., Demleitner M., Schilbach E., 2010, AJ, 139, 2440
Schlegel D. J., Finkbeiner D. P., Davis M., 1998, ApJ, 500, 525
Seabroke G. M., Gilmore G., 2007, MNRAS, 380, 1348
Serenelli A. M., Althaus L. G., Rohrmann R. D., Benvenuto O. G., 2001, MNRAS, 325, 607
Sion E. M., Fritz M. L., McMullin J. P., Lallo M. D., 1988, AJ, 96, 251
Tremblay P.-E., Bergeron P., Gianninas A., 2011, ApJ, 730, 128
Vennes S., 1999, ApJ, 525, 995
Wielen R., 1977, A&A, 60, 263
Wood M. A., 1995, in Koester D., Werner K., eds, Lecture Notes in Physics Vol. 443, White Dwarfs. Springer Verlag, Berlin, p. 41

APPENDIX A: LIKELIHOODS

Here we give our expressions for the proper motion likelihoods of an individual object. These largely follow Ratnatunga, Bahcall & Casertano (1989), modified to include errors in proper motion. We ignore errors in the sky position (ℓ, b), which are small.

Assuming a Schwarzschild distribution function, then, in coordinates aligned with the principle axes of the velocity ellipsoid,

$$f(\boldsymbol{V}) = \frac{1}{\sqrt{8\pi^3}\sigma_1\sigma_2\sigma_3} \exp\left(-(\boldsymbol{V}-\boldsymbol{V_0})^{\mathrm{T}} \cdot \boldsymbol{\Gamma} \cdot (\boldsymbol{V}-\boldsymbol{V_0})\right), \tag{A1}$$

where $\boldsymbol{\Gamma} = \mathrm{diag}(1/2\sigma_1, 1/2\sigma_2, 1/2\sigma_3)$ and $\boldsymbol{V_0}$ is the mean velocity. Ignoring errors in distance, we then rotate to axes aligned with the sky plane, and integrate over the unobserved radial velocity, which, in this case, is a nuisance parameter.

We define, $\boldsymbol{\Lambda}$, to be the dispersion tensor rotated into the coordinate system, (ℓ, b, d), aligned with the sky plane. This will be given by $\boldsymbol{\Lambda} = \mathbf{R} \cdot \boldsymbol{\Gamma}$, where $\mathbf{R}$ is a rotation matrix (given explicitly as equation A4 in Ratnatunga et al. 1989). The probability distribution, after integrating over the radial velocity as a nuisance parameter, is an ellipsoid in the sky plane

$$p(v_l, v_b) = C' \exp\Big[-\alpha(v_\ell - \bar{v_\ell})^2 - \beta(v_b - \bar{v_b})^2 - 2\gamma(v_\ell - \bar{v_\ell})(v_b - \bar{v_b})\Big], \tag{A2}$$

where $\bar{v_\ell}$ and $\bar{v_\ell}$ are the components of $\boldsymbol{V_0}$ in the directions of l and b (which can be obtained via $(\bar{v_\ell}, \bar{v_b}, \bar{v_d}) = \mathbf{R} \cdot \boldsymbol{V_0}$) and α, β, γ and C' are given by

$$\alpha = \Lambda_{22} - \Lambda_{12}^2/\Lambda_{11}, \tag{A3}$$

$$\beta = \Lambda_{33} - \Lambda_{13}^2/\Lambda_{11}, \tag{A4}$$

$$\gamma = \Lambda_{23} - \Lambda_{12}\Lambda_{13}/\Lambda_{11}, \tag{A5}$$

$$C' = \sqrt{\alpha\beta - \gamma^2}/\pi. \tag{A6}$$

For each object, we have measurements of v_l and v_b, together with an associated velocity error σ. Integrating over the 'true' v_l and v_b gives the log likelihood used in equation (9) as

$$\begin{aligned}\log \mathcal{L}_i(v_\ell^{\mathrm{obs}}, v_b^{\mathrm{obs}}) &\equiv \log \int \mathrm{d}\boldsymbol{V}\, f(\boldsymbol{V}) P\left(\boldsymbol{V} | v_\ell^{\mathrm{obs}}, v_b^{\mathrm{obs}}, \sigma\right) \\ &= \log C'' - \frac{\delta}{(\alpha+\delta)(\beta+\delta)-\gamma^2} \\ &\quad \times \Big[(\Delta v_b^2 + \Delta v_\ell^2)(\alpha\beta - \gamma^2) \\ &\quad + \delta\left(\beta\Delta v_b^2 + \alpha\Delta v_\ell^2 + 2\gamma\Delta v_\ell \Delta v_b\right)\Big],\end{aligned} \tag{A7}$$

where

$$\delta = 1/2\sigma^2, \tag{A8}$$

$$\Delta v_\ell = v_\ell^{\mathrm{obs}} - \bar{v_\ell}, \tag{A9}$$

$$\Delta v_b = v_b^{\mathrm{obs}} - \bar{v_b}, \tag{A10}$$

$$C'' = C' \frac{\delta}{\sqrt{\pi}\sqrt{(\alpha+\delta)(\beta+\delta)-\gamma^2}} \tag{A11}$$

$$= \delta \sqrt{\frac{\alpha\beta - \gamma^2}{\pi^3[(\alpha+\delta)(\beta+\delta)-\gamma^2]}}. \tag{A12}$$

Note that for small error, $\delta \to \infty$, and equation (A7) reduces to the log of equation (A2) as expected.

This paper has been typeset from a TEX/LATEX file prepared by the author.